Electronic Supplementary Material (ESI) for Soft Matter.

Supporting Information

Multiplexed and Continuous Microfluidic Sensors using Dynamic Complex Droplets

Baishali Barua, Tyler J. Durkin, Isabel M. Beeley, Aakanksha Gadh, and Suchol Savagatrup*

Department of Chemical and Environmental Engineering, the University of Arizona
1133 E. James E. Rogers Way, Tucson Arizona 85721

*Author to whom correspondence should be addressed: suchol@arizona.edu

Keywords: complex emulsions, interfacial tensions, PDMS microfluidics, multiplexed, real-time, sensors

Table of Contents

1. Material & Methods

1.1 Chemicals

Toluene, ortho-dichlorobenzene (ODCB), perfluorotributylamine (FC-43), sodium dodecylsulfate (SDS, ≥99%), and polystyrene-*block*-polyacrylic acid (PS-*b*-PAA) were obtained from Sigma-Aldrich. Capstone FS-30 (25% solids in water) was obtained from Chemours and 2-trifluoromethyl-3-ethoxyperfluorohexane (HFE-7500) was obtained from Santa Cruz Biotechnology. All chemicals were used as received. Surfactant solutions were prepared by dissolving SDS or Capstone in Milli-Q water at concentrations of 1 wt%, 0.5 wt%, and 0.1 wt%, depending on the desired droplet configuration (*e.g.*, Janus or double emulsion). The fluorescent dyes perylene (≥ 99%) and coumarin 545T (≥ 98%) were purchased from Fisher Scientific. N,N'-Bis(2,6-diisopropylphenyl)-1,6,7,12-tetraphenoxy-3,4,9,10-perylenetetracarboxylic Diimide (lumogen Red F300) was purchased from TCI Chemicals. Negative photoresist SU-8 2150 was purchased from Fisher Scientific. SYLGARD 184, a two-component system, poly(dimethylsiloxane) base and a curing agent was obtained from Dow Chemical.

1.2 Instruments

The top-view optical micrographs of droplets were imaged using an AmScope Inverted Microscope. Bright-field and fluorescent images were taken with a Leica DMi8 Fluorescent Microscope. For use in directional emission experiments and for optical and fluorescent images, droplets were deposited on glass coverslips attached to a Thermo-Fisher Scientific Invitrogen Attofluor Cell Chamber to enable the droplets to be arranged in a uniform monolayer. Emission spectra were acquired with an AVANTES AvaSpec 2048-L Spectrophotometer equipped with an AVANTES AvaLight-HPLED as the excitation source ($\lambda = 405\ nm$) and a Bifurcated Optical Fiber allowing the light to be directed to the droplets vertically and capture emitted light directed straight

upward. Finally, analyte solutions were injected inside the microfluidic channels using Harvard Apparatus PHD ULTRA™ CP Syringe Pumps.

1.3 Emission wavelengths of fluorescent dyes

All fluorescent dyes were dissolved in toluene at the concentration of 0.25M, at which we achieved a defined emission peak. A bifurcated optical fiber connected with a UV light and a spectrophotometer was used to record the emission wavelength of three dyes.

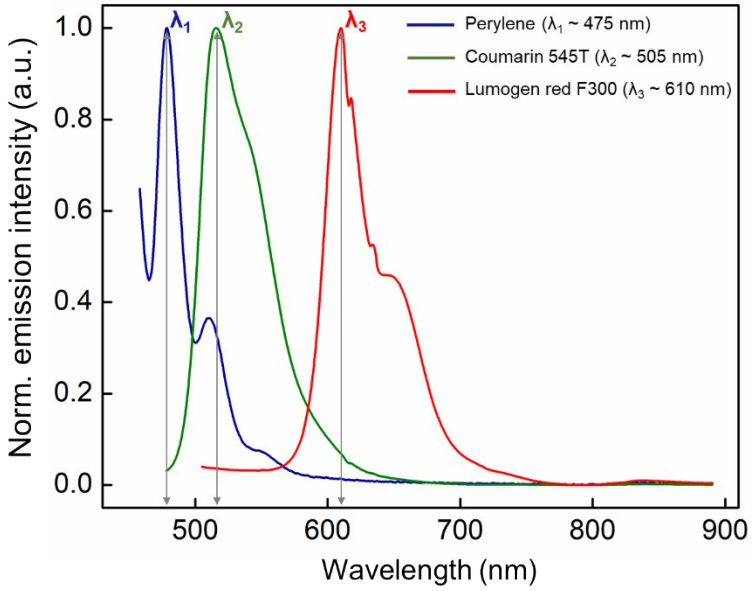

Figure S1. Experimental emission spectra of three fluorescent dyes – perylene (λ_1~475 nm), coumarin 545T (λ_2~505 nm), and lumogen red F300(λ_3~610 nm). These three dyes were chosen based on their emission wavelengths to allow the recording of emission intensities generated from differentially formulated droplets.

2. Fabrication of emissive droplets

2.1 Emissive complex droplets

We followed an emulsification method to fabricate monodispersed complex droplets comprised hydrocarbon oil (H-oil) and fluorocarbon oil (F-oil) phases reported by Zarzar et al.[1] An aqueous solution of 1 wt% SDS was used as the continuous phase for the fabrication of monodispersed droplets of various sizes. The dispersed phase containing equal volume of toluene

with a fluorescent dye as H-oil and a 9:1 mixture of HFE-7500 and FC-43 as F-oil was kept above the upper critical temperature (T_c = 32°C) to induce miscibility during emulsification. The ratio of HFE-7500 and FC-43 was chosen to tune the critical temperature (T_c) at which H-oil and F-oil is miscible as well as to promote complete phase separation at room temperature.[2] We used the Dolomite Microfluidics

setup inside an incubator to maintain the temperature above T_c (>32°C) throughout the fabrication process. Specifically, two Mitos P pressure pumps were used to control the flow rates of the continuous phase and dispersed phase and both phases were driven by pressurizing the 30 mL chambers with N_2 to provide steady and stable flow into the flow-focusing chip, Telos 2 Reagent Chip (50 μm). After emulsification, the droplets were cooled to room temperature to produce double emulsions with equal volumes of the H-oil and F-oil phase through phase separation. Optical micrographs of the droplets were used in conjunction with static image analysis to determine the diameter and dispersity of the droplets through a MATLAB code.

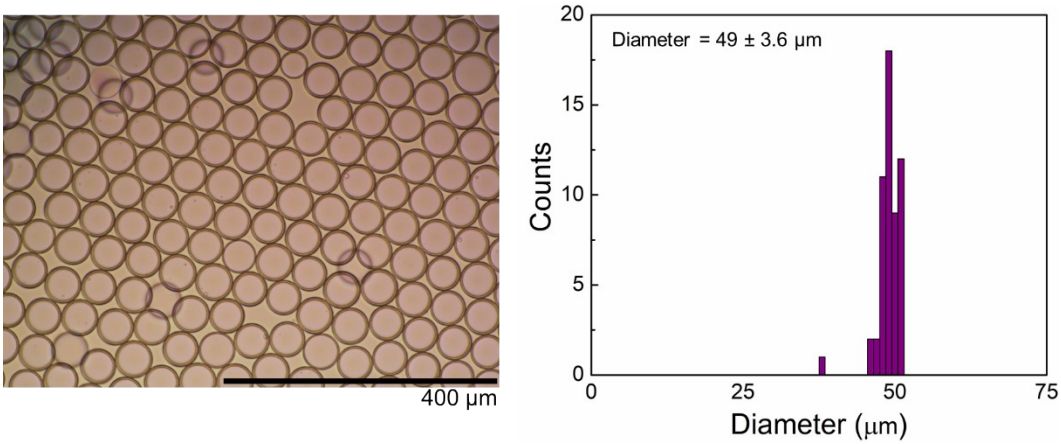

Figure S2. Optical micrograph of monodispersed complex droplets fabricated using Dolomite Microfluidics Setup. Droplet size (diameter) and standard deviation was assessed using a MATLAB code.

2.2 Single-phase droplets

We used ortho-dichlorobenzene (ODCB) as dispersed phase and 1 wt% SDS solution as continuous phase for the fabrication of single-phase droplets to be used for control experiments. We followed the same process described in section 2.1 for generating monodispersed droplets using Dolomite microfluidics.

2.3 Complex droplets containing PS-*b*-PAA

Furthermore, for the preparation of PS-b-PAA functionalized complex emulsions, PS-*b*-PAA with the ratios of molecular weights of 3:5 kDa (PS to PAA) was dissolved in the fluorescent dye-containing toluene and used as the H-oil phase. The F-oil phase was identical to earlier studies, containing HFE-7500 and FC-43 at 9:1 ratio. We followed the same fabrication method using Dolomite Microfluidics to generate monodispersed droplets containing PS-*b*-PAA. Monodispersed droplets were chosen to effectively mitigate the effects of droplet size on the optical properties that are inherent to an array of droplets with varying diameters (polydispersed). Specifically, Zeininger et al. reported that the normalized change in optical properties and emission intensity are consistent across droplets with different diameters and are only a function of the internal morphology, but the range of absolute emission intensity depends on the size of the droplets.[2] Thus, the signal could be confounded when collecting emissions from polydispersed samples without additional internal references.[2] Furthermore, the choice of approximately 50 μm for the droplet diameter was twofold: first, the ease of their application into microfluidic-based sensors and second, increased stability when compared to smaller droplets. Specifically, they can be easily injected into the microwell and can remain stable for the extended duration of the experiments while droplets with smaller diameters were found to both coalesce and burst at faster rates.

3. **Fabrication of PDMS microfluidic devices**

PDMS microstructures with different patterns were fabricated using the standard soft lithography (replica modelling) method.[3–5] Initially, we prepared silicon wafers by cleaning with piranha solution (H_2SO_4+H_2O_2 at a ratio of 3:1) and then dried off with clean air. The cleaned and dried wafers were then put on a hot plate at 95℃ for 15 minutes. Next, the prepared wafer was coated with a thin film of SU-8 2150 photoresist by using a spin coater at 3000 rpm for 1 minute. The coated silicon wafer was baked on hot plate at 65℃ for 5 minutes and 95℃ for 10 minutes. Then, the wafers were exposed under the UV light with wavelength of 365 nm using a mask aligner to imbue the photoresist with a relevant pattern. Finally, the wafers were again baked (65℃ for 5 minutes, 95℃ for 10 minutes and 65℃ for 5 minutes again) and then washed with a developer solution PGMEA (Propylene glycol monomethyl ether acetate) to remove any unexposed SU-8. After rinsing the wafer with isopropyl alcohol, SU-8 molds were formed.

Next, PDMS is used to make microchannel structures. The hardness of the structures can be controlled by using different ratios of silicon elastomer and curing agent. Therefore, we adopted a ratio of 10:1 by weight to make microchannel layers and did so by pouring well mixed PDMS solution onto the patterned silicon wafer and immediately moving the wafers into a vacuum to remove any air bubbles created during the mixing process. Then, after remaining at room temperature for 36-48 hours, the curing PDMS replica was peeled off from the wafer. Subsequently holes were punched into the PDMS slab using disposable biopsy punch to create the desired design of the microfluidic devices.

Furthermore, we bonded the PDMS pieces to glass slides using AutoGlow plasma system. The plasma treatment modifies the surface chemicals and allows the PDMS with the channels to

stick against other substrates. Before binding, we cleaned the PDMS pieces and glass surface to confirm the strong and permanent bonding.

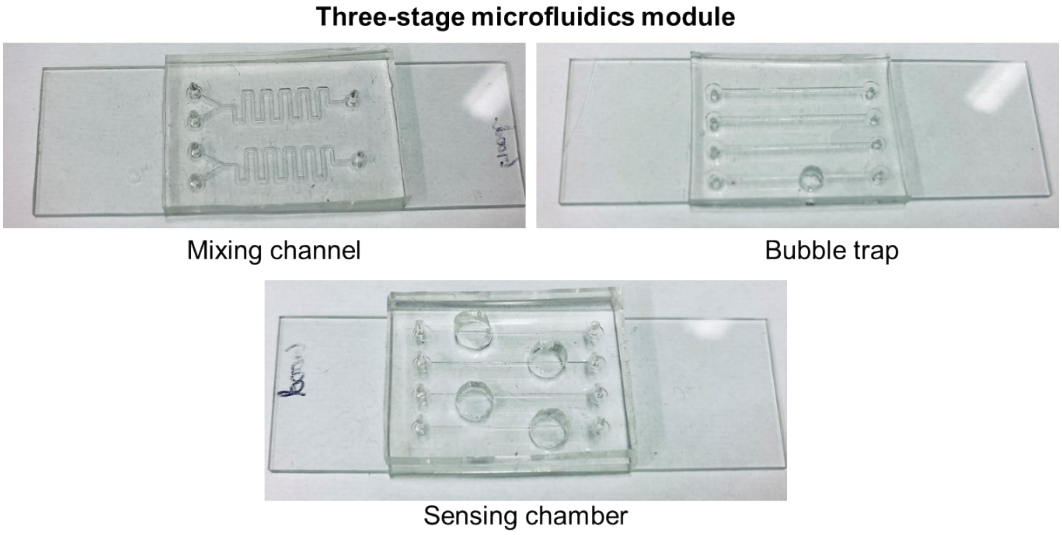

Figure S3. Images of PDMS pieces made by soft lithography process to build the three-stage microfluidics module for real-time and continuous monitoring.

4. **Determination of calibration curve for directional emission**

To determine the calibration curve for directional emission (*i.e.* the emission intensity as a function of the droplet morphology) of the emissive complex droplets, 40 mL of prefabricated monodispersed droplets were deposited into 60 mL of 0.5 wt% surfactant solution. Next, we added 300 mL of surfactant solutions, each containing different ratios of SDS and Capstone. The optical fiber was placed above the monodispersed droplet monolayers. The UV light through the optical fiber was incident vertically above the droplets to capture the amount of emitted light coming straight upward and omit all interference from the surrounding. The distance between droplet and optical fiber was maintained at 14 mm for all data collection. In each experiment, the glass surface of the sample holder was wetted with surfactant solution before the droplets were deposited into said solution in the middle of the chamber. Due to gravity, the droplets spread and ultimately align in a monolayer. Once the monolayer was formed, we recorded the emission intensity of the dyes

at their characteristic wavelengths. All sensing experiments were performed using monodispersed (diameter ~ 50 μm) droplets, to eliminate size effects on emission read-out (in the size-region of macroemulsions). Additionally, only monodisperse droplets arrange in a hexagonally packed reproducible monolayer on the flat glass surface, thus leading to consistent emission intensities.

First, we collected emission signals for complex droplets with perylene dye and measured intensity at ~ 475 nm. For perylene, we used the secondary peak at 475 nm, instead of its maximum peak at 410 nm, to avoid interference from the excitation wavelength of 405 nm. Additionally, we conducted the same experiment for complex droplets with coumarin 545T (at ~505 nm) and lumogen red F300 (at ~610 nm). All the data points were normalized to the emission intensity of the droplets.

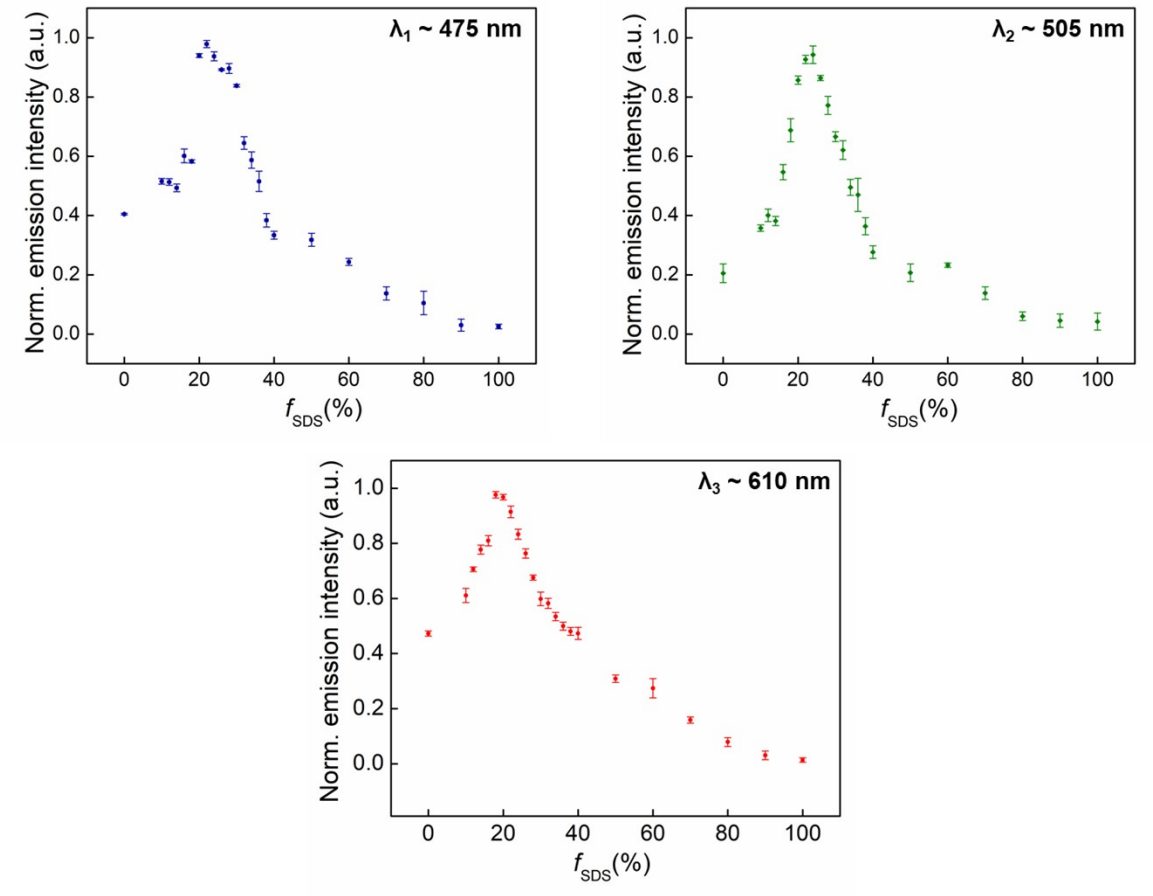

Figure S4. Emission intensity as a function of f_{SDS}. The maximum intensity occured when f_{SDS} is approximately 0.20. The three plots represent complex droplets with perylene, coumarin 545T, and lumogen red F300 dissolved in the H-oil. Complex droplets exhibit similar dynamic behavior

in all three experiments, irrespective of the type of fluorescent dye. The error bars (vertical bars inside the markers) represent the standard deviations of repeated measurements ($N \geq 5$)

5. Normalization of experimental data sets

The goal of normalizing datasets is to transform features to be on a similar scale. We measured the minimum and maximum emission intensity for each formulation of droplets. These two values were then used to normalize the other measurements in the same experimental data set, using the following equation:

$$I_{normalized} = \frac{I_{measured} - I_{min}}{I_{max} - I_{min}}$$

We chose the use of normalized emission because the raw values of emission intensity can be influenced by several experimental variables. The use of normalized intensity provided a method to incorporate internal references and to effectively compare between experiments.

6. Mixing efficiency of microfluidic channels

Typical fluid flow in microfluidic channels is laminar, due to the relatively low hydraulic diameter and low flow velocity. This hinders the effective mixing between liquid-liquid phases. We tested the efficiency of a serpentine mixing channel to ensure complete mixing of inlet liquid streams from multiple syringe pumps. To elaborate, the edges of the serpentine microchannels induced mixing of different liquids before entering into the next stages - bubble trap and sensing chamber. Optical microscope images of different sections of mixing channels and sensing chamber were recorded to confirm the perfect mixing in the mixing channels.

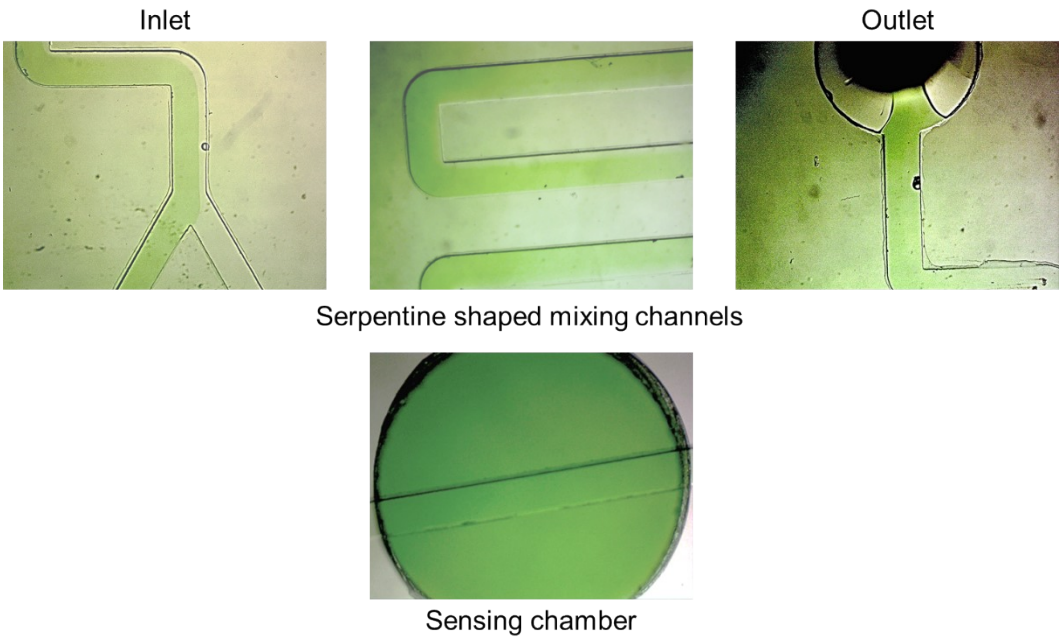

Figure S5. Microscope images of mixing channels and sensing chamber to ensure the complete mixing of multiple liquid streams. We used dyed water to confirm the uniform mixing in the microchannels.

7. Design optimization of microfluidics module

We optimized the geometry of the PDMS microwell (sensing chamber) as well as the inlet liquid flowrates to improve performance of the sensing platform. We considered two significant factors during optimization: (1) stability of the droplets inside the sensing chamber to produce consistent sensing signals (*i.e.*, changes in fluorescent emission intensity) and (2) response time: time to achieve consistent sensing output. Thus, we tested with sensing chamber of three different diameters – 1.5 mm, 3 mm, and 5 mm at three different total flowrates (150 µL min^{-1}, 200 µL min^{-1}, and 200 µL min^{-1}). Despite at higher flowrate of the liquid streams decreased the response time, we observed that such conditions reduced the stability of the droplets and decreased the reproducibility of the optical signals. Specifically, higher flowrate created agitations, thus

movement in the droplets, which in turn increased stabilization time and led to noisy and unstable emission signals. Moreover, liquid entering at high flowrates caused droplets to burst and coalesce inside the chamber, which induced inconsistency in the signal. However, lower flow rates significantly increased the response time (amount of time to reach equilibrium). To remedy these competing concerns, we evaluated the performance of the microfluidics setup comparing the response time and ΔI (where, $I_H = higher\ emission, I_L = lower\ emission$) by adjusting the two design parameters. We observed that a residence time of 2 minutes at total flow rate of 200 µL min^{-1} for the sensing chamber with 5 mm diameter was ideal for our experiments.

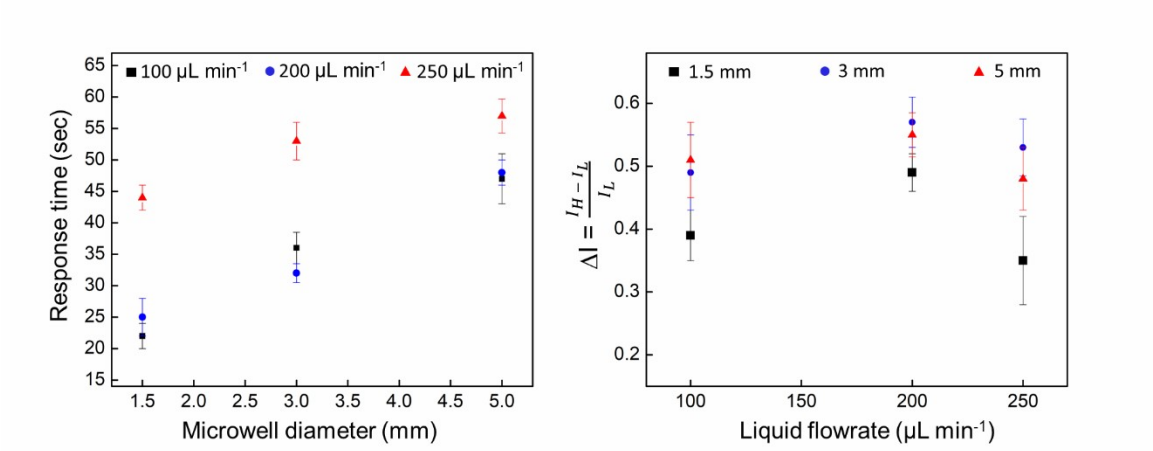

Figure S6. Sensing chamber diameter, inlet liquid total flowrate, flow time were optimized to record continuous emission signal.

8. Real-time, Continuous sensing

Our first set of experiments focused on the transition of emissive complex droplets with perylene dye from pure SDS solution ($f_{SDS} \approx 1$) to pure Capstone solution ($f_{SDS} \approx 0$). When $f_{SDS} \approx 1$, $\gamma_H < \gamma_F$ in SDS solution, droplet morphology was F/H/W. We observed that this initial morphology exhibited the lowest emission intensity, which was consistent with previous reports. Thus, we used this value as the baseline for the minimum emission. The opposite phenomena

happened at f_{SDS} 0, droplets were changed to H/F/W configuration and produced higher emission signal. We tracked the emission intensity of droplets with perylene dye. We performed similar experiments using complex droplets with coumarin 545T and lumogen red F300 and observed consistencies in the dynamic and reversible behavior over 10 cycles.

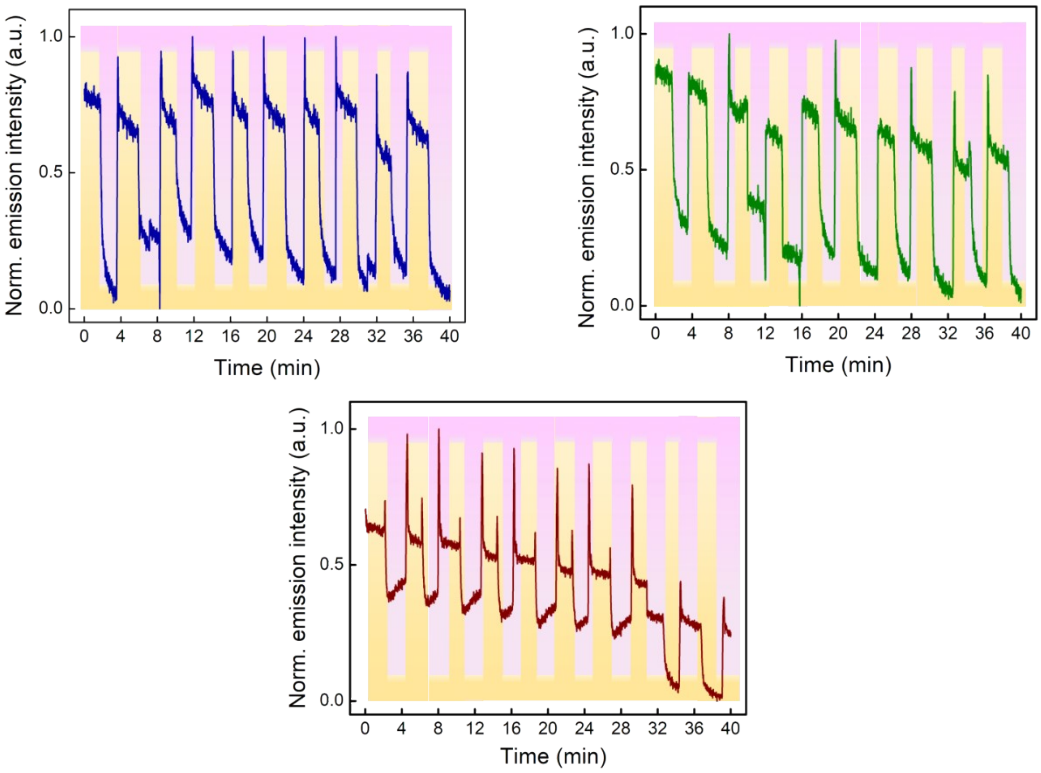

Figure S7. Continuous emission signals of the complex droplets. SDS and Capstone amount was alternated over total 10 cycles to observe the dynamic response produced by droplets.

9. pH responsiveness of PS-*b*-PAA functionalized complex droplets

We investigated the effect of conformation of PS-*b*-PAA on interfacial tension. Particularly, the conformation of PAA depends on the pH of its surrounding phase. At low pH, PAA exists in a compact globule, and as pH increases the polymer is ionized and extends into an open coil.[6] This conformational change affected the ability of PS-*b*-PAA to reduce interfacial tension of a H-oil/water interface as PAA in a globule is less surface active than PAA in a coil.[7–9]

The composition of PS-*b*-PAA dissolved in the H-oil phase was 3:5 kDa, proven to be an effective polymeric surfactant at the H-oil/water interface. We began with the complex droplets functionalized with PS-*b*-PAA and initialized with Capstone solution of pH 12. At higher pH, PS-*b*-PAA acted as an effective hydrocarbon surfactant and decreases γ_H. Thus, the morphological state was F/H/W and emission intensity was lower because of the upward internal curvature of the H-oil/F-oil interface. Next, we lowered the pH value of Capstone solution to pH 3, when the PS-*b*-PAA surfactant changes conformation and is rendered less effective and caused the morphological inversion of the complex emulsions. Thus, the F-oil phase began to shift to comprise the outer phase of the double emulsion (*i.e.*, H/F/W), which caused a rapid increase in emission value. As a following step, we changed the analyte to SDS solution and observed morphological inversion leading to lower emission intensity. This result indicated that PS-*b*-PAA is a more effective surfactant under basic pH. This demonstration is an important validation that the PS-*b*-PAA anchored at the interface of oil and water can be modulated through physical conformational changes to affect interfacial tensions, potentially serving as a sensing mechanism at the interface of complex droplets.

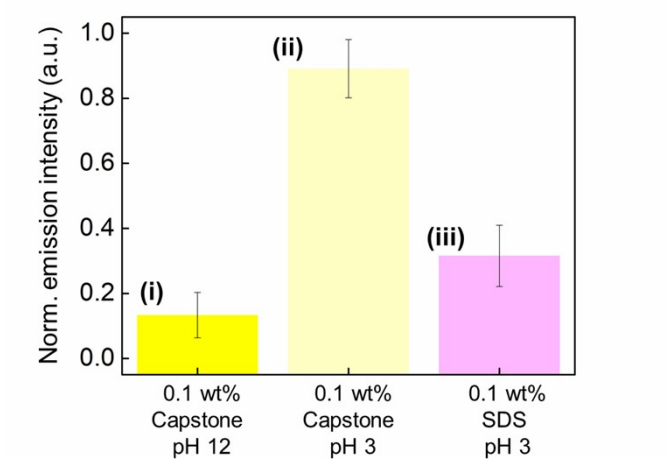

Figure S8. Demonstration of PS-*b*-PAA effectiveness as a polymeric surfactant. It was dissolved in toluene before producing the complex droplets. By tuning pH, the effectivity of this surfactant on the interfacial tensions was quantified.

References

(1) Zarzar, L. D.; Sresht, V.; Sletten, E. M.; Kalow, J. A.; Blankschtein, D.; Swager, T. M. Dynamically Reconfigurable Complex Emulsions via Tunable Interfacial Tensions. *Nature* **2015**, *518* (7540), 520–524. https://doi.org/10.1038/nature14168.

(2) Zeininger, L.; Nagelberg, S.; Harvey, K. S.; Savagatrup, S.; Herbert, M. B.; Yoshinaga, K.; Capobianco, J. A.; Kolle, M.; Swager, T. M. Rapid Detection of Salmonella Enterica via Directional Emission from Carbohydrate-Functionalized Dynamic Double Emulsions. *ACS Cent. Sci.* **2019**, *5* (5), 789–795. https://doi.org/10.1021/acscentsci.9b00059.

(3) Kim, P.; Kwon, K. W.; Park, M. C.; Lee, S. H.; Kim, S. M.; Suh, K. Y. Soft Lithography for Microfluidics: A Review. *Biochip J.* **2008**, *2* (1), 1–11.

(4) Friend, J.; Yeo, L. Fabrication of Microfluidic Devices Using Polydimethylsiloxane. *Biomicrofluidics* **2010**, *4* (2). https://doi.org/10.1063/1.3259624.

(5) Raj M, K.; Chakraborty, S. PDMS Microfluidics: A Mini Review. *J. Appl. Polym. Sci.* **2020**, *137* (27), 1–14. https://doi.org/10.1002/app.48958.

(6) Chen, Q.; Vancso, G. J. PH Dependent Elasticity of Polystyrene-Block-Poly(Acrylic Acid) Vesicle Shell Membranes by Atomic Force Microscopy. *Macromolecular Rapid Communications*. 2011, pp 1704–1709. https://doi.org/10.1002/marc.201100332.

(7) Choucair, A.; Lavigueur, C.; Eisenberg, A. Polystyrene-b-Poly(Acrylic Acid) Vesicle Size Control Using Solution Properties and Hydrophilic Block Length. *Langmuir* **2004**, *20* (10), 3894–3900. https://doi.org/10.1021/la035924p.

(8) Lee, H. il; Boyce, J. R.; Nese, A.; Sheiko, S. S.; Matyjaszewski, K. PH-Induced Conformational Changes of Loosely Grafted Molecular Brushes Containing Poly(Acrylic Acid) Side Chains. *Polymer (Guildf).* **2008**, *49* (25), 5490–5496. https://doi.org/10.1016/j.polymer.2008.10.001.

(9) Sparks, D. J.; Romero-González, M. E.; El-Taboni, E.; Freeman, C. L.; Hall, S. A.; Kakonyi, G.; Swanson, L.; Banwart, S. A.; Harding, J. H. Adsorption of Poly Acrylic Acid onto the Surface of Calcite: An Experimental and Simulation Study. *Phys. Chem. Chem. Phys.* **2015**, *17* (41), 27357–27365. https://doi.org/10.1039/c5cp00945f.